

DEVELOPMENT OF A SELF-STABLE SUPERCONDUCTING MAGNETIC BEARING FOR HIGH-SPEED ELECTRIC MOTORS

Copyright Material PCIC energy
Paper No. PCIC energy EUR25_15

Gabriel Storti WEG Jaraguá do Sul Brazil storti@weg.net	Fredemar Rüncos WEG Jaraguá do Sul Brazil fredemar@weg.net	Richard Stephan UFRJ Rio de Janeiro Brazil richard@dee.ufrj.br	Elkin Rodriguez UFRJ Rio de Janeiro Brazil elkin@dee.ufrj.br	Paulo Branco ULisboa Lisboa Portugal pbranco@tecnico.ulisboa.pt
---	--	--	--	---

Abstract - Addressing the urgent need to mitigate climate change, industries are shifting towards cleaner energy solutions. Electric drives in the oil and gas industry, as well as in the green hydrogen sector, demand high-speed electric machines making bearings a critical component. In high-speed machines, dynamic stability and low friction are essential for optimal performance. For high-speed drives, magnetic bearings emerge as an effective solution. This paper provides the theoretical basis of a passive superconducting magnetic bearing (PSMB), describes its manufacturing process, and demonstrates its application in a 10kW high-speed electric motor. Experimental results are presented for two configurations: direct grid connection using a sine wave voltage source and operation with a PWM variable speed drive (VSD) inverter. The self-dynamic stability of the rotor is demonstrated as it passes through the rotor's critical speeds. Advancements in superconducting technology and cryogenics offer promising opportunities for disruptive solutions. Finally, the advantages and limitations of PSMBs are discussed.

Index Terms — Magnetic bearings, Superconductors, Cryogenic.

I. INTRODUCTION

In order to meet the requirements of the Paris Climate Agreement, industries need to adapt their energy-intensive processes.

Energy-intensive industrial drives are the focus of this change. Today, many power drives, especially in the oil and gas industry, still use steam turbines, gas turbines and, in some cases, internal combustion engines [1]. All these solutions do not meet the requirements of the Paris agreement, and industry needs to replace them by electric drives that can use clean and renewable energy sources.

As the drives are high-powered and high-speed, they need to be displaced by electric motors that have these characteristics, i.e., high-speed motors [2]. The speed of the motors can reach several krpm, even close to 50krpm.

These speed levels present several technological challenges that need to be taken into account when designing these motors. One of these challenges is the bearings, which need to be suitable for the speed and load condition of the drive.

The current state of the art offers Active Magnetic Bearings [AMB] as a solution for high-speed motors once there is no mechanical contact, and they are an oil-free solution. However, AMBs need to be parameterized for the drive conditions and are totally dependent on the control panel's power supply. This means that the bearing operator needs to have a good knowledge of bearing control, and in the event of a power failure, the bearing lands, which

requires more care and protection. The complexity of this solution highly depends on the magnetic bearing supplier and the design phase, considering the loads and operating range. For instance, when it is necessary to operate the equipment under different conditions not previously indicated, the magnetic bearing should be tuned, within certain limits, by the OEM, end user, or even the bearing supplier, as the solution is often considered a "black box", which can be a source of concern for the industry.

As an alternative to the AMB, there is the possibility of developing a Passive Superconducting Magnetic Bearing (PSMB) for high-speed electrical motors [HSEM]. This solution would focus on medium voltage applications, such as 15MW - 15krpm, or even larger and faster HSEM systems.

The PSMB has the advantage of not needing a control panel because it is self-controlled and does not depend on the power supply for its operation. The self-stable condition is pretty similar to the well-known sleeve bearings solution, with the advantage being oil-free and low friction. However, a nitrogen cryostat is required to cool the superconductor. Additionally, it does not need an axial bearing because the superconductor maintains the rotor's axial position.

This paper will show the design, construction, and test results of a passive magnetic bearing for a 10kW-2pole motor. The tests were carried out for the motor operating without and with load coupling, where the results show that the PSMB solution can be a reliable alternative. It will be shown that the technological challenge of the solution lies in the design and construction of the cryostat.

II. SHORT THEORETICAL BACKGROUND

Nowadays, magnetic forces can be applied to support the rotors of various types of rotating machines without the friction associated with traditional mechanical bearings. The utilization of magnetic forces has been enabled by developments in the late 20th century in power electronics, microelectronics, current and position sensors, magnetic materials, and superconductors.

The vast majority of the so-called Magnetic Bearings available in the industry are based on the controlled attraction forces between electromagnets and ferromagnetic materials (EML method). There are also Magnetic Bearings that utilize repulsion forces between magnetic fields of the same polarity (EDL method) and, finally, those based on the stable interaction between type II superconductors and permanent magnets (SML method) [3, 4]. Fig. 1 summarizes these methods.

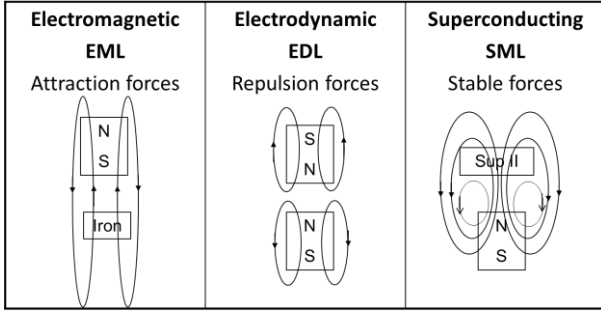


Fig. 1 The main types of Magnetic Bearings

Although all three types of levitation are applied in MagLev trains [5], the EDL and SML methods have not yet reached the same Technological Readiness Level (TRL) [6] as the EML method for Magnetic Bearings due to airgap constraints. This paper describes efforts to achieve TRL 5 for a Superconducting Magnetic Bearing, emphasizing the advantages of stable forces while addressing the challenges of refrigeration required for superconductors.

A. Superconducting Magnetic Bearing: Finite Element (FE) Simulations for Its Design

The cylindrical cross-sectional view of the PMSB along the z - r plane, highlighting its geometry and principal components, is shown in Fig. 2. All critical dimensions are labeled in millimeters. The rotor comprises a steel shaft and a stainless-steel sleeve situated between the shaft and the permanent magnet (NdFeB)/Fe assembly, which also mitigates any magnetic field deviations while offering structural reinforcement. The nine permanent magnet (PM) rings are organized in a Halbach array configuration [7], with their magnetization direction shown in Fig. 2 as blue arrows. Additionally, four magnetic iron (Fe) rings are incorporated as radial flux concentrators to enhance the magnetic field interacting with the three YBCO rings. These YBCO rings are situated in the stator and are responsible for levitating the rotor. The Fig. 2 was subsequently utilized in the finite element (FE) simulations to aid in the bearing design.

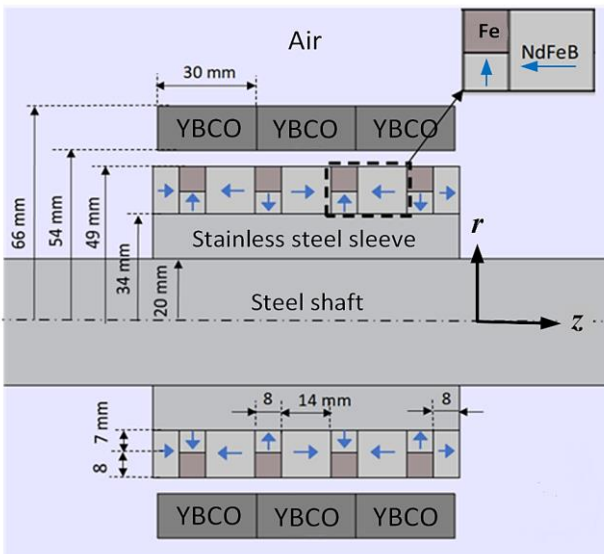


Fig. 2 Finite element (FE) design geometry and materials utilized, illustrating symmetry around the z -axis.

Fig. 3 shows the magnetization curve considered for the iron rings, the AISI 1020 steel. To model the YBCO material when in the superconducting state, consider relation (1) between current density J and electric field E for type II superconductors [7]. Parameter J_c represents the critical current density that, according to the Kim-Anderson model [8], depends on the penetrating flux density B , as shown in relation (2).

$$E = E_0 \left(\frac{J}{J_c} \right)^n, \quad (1)$$

$$J_c = J_{c0} \frac{B_0}{B_0 + |B|} \quad (2)$$

For the YBCO, the following parameters were used: $n = 21$, $E_0 = 1 \times 10^{-4} \text{ Vm}^{-1}$ and $B_0 = 0.1 \text{ T}$ [9]. Based on previous results [10], the critical current density in the absence of a field was set to $J_{c0} = 8 \times 10^7 \text{ Am}^{-2}$. In all simulations, the following three values of remanent flux density B_r were considered for PMs: 1.17 T (N35), 1.25 T (N40), and 1.32 T (N45).

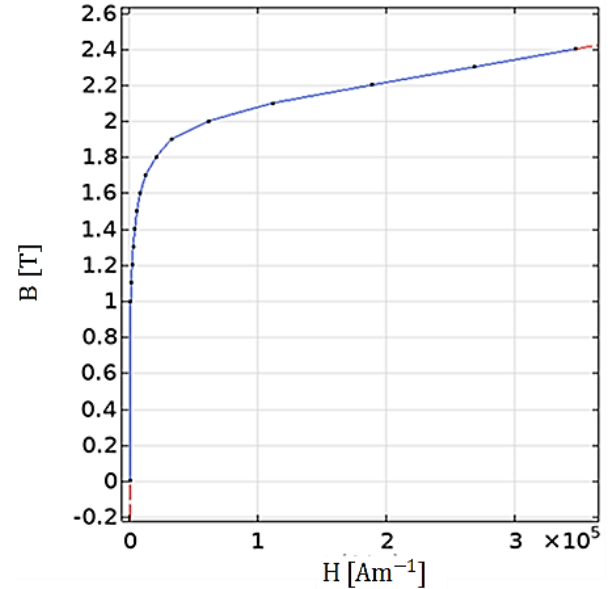


Fig. 3 Fe magnetization curve for radial flux concentrators.

The 2D FE simulations facilitate the determination of the PSMB's magnetic field distribution and the current density within the YBCO material. Initially, the magnetization of the YBCO rings was simulated, accounting for their Field Cooling (FC) process. This simulation involved two FE steps to model the system's behavior accurately. They were:

1) The upper portion of the rotor (NdFeB + Fe) is first moved toward the group of YBCO rings to their "cooling height", $r = +h_a$ (Fig. 4a) and simulated.

2) In the second simulation step, the upper section of the rotor is moved away from the field-cooled YBCO rings to reach its final "levitation height", creating an air gap, g_a , (Fig. 4b).

Field cooling (magnetization) with the rotor positioned above the central position ($h_a > 0$), according to Fig. 4a, allows for stronger magnetic field penetration in the upper bearing (YBCO rings' zone). In the second phase of magnetization, levitation forces from the lower bearing zone push the rotor upwards, moving to the central position. Hence, the levitation force must balance the gravitational one to keep the rotor levitating at its central axis.

The distribution of the current density J in the superconductors during their magnetization process is shown in Fig. 4a. It also depicts the field distribution generated after the rotor is moved upward by a mechanical device to rotor jacking and after the Field Cooling (FC) process of the superconductors, which includes a vertical offset of the rotor, $h_a > 0$. Fig. 4b presents the distribution of the magnetization current density in the YBCO rings and the resulting magnetic field during the second magnetization phase after the rotor is finally positioned such that its axis aligns with the stator axis.

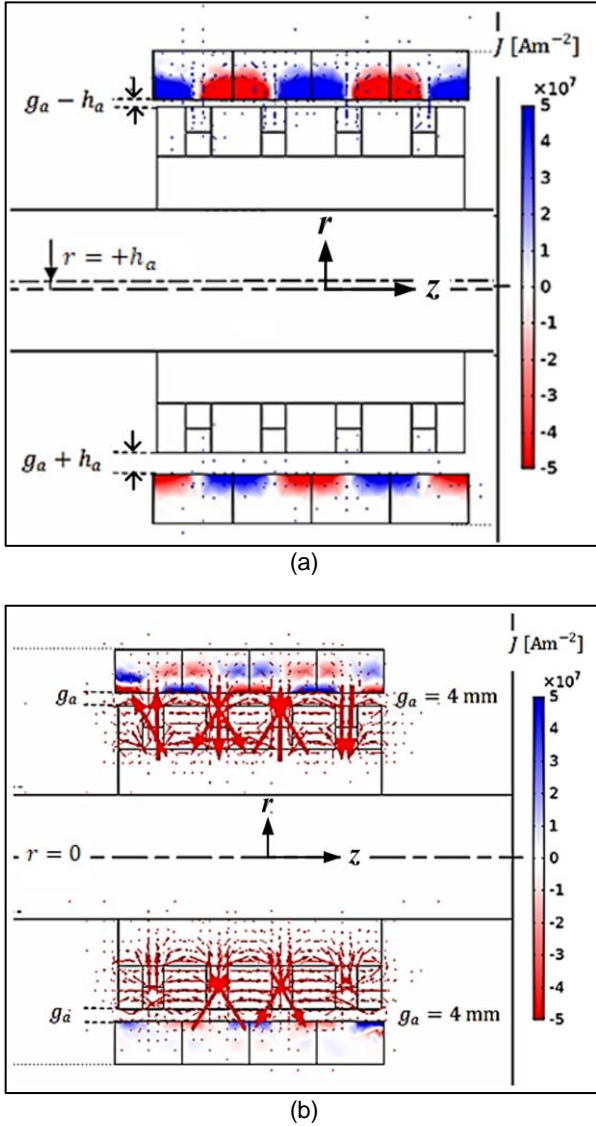


Fig. 4 Distribution of current density and magnetic field after (a) the first step of magnetization and (b) when the rotor becomes located at its center.

1) *Vertical levitation forces*: the 2D FE simulations produced a certain levitation magnetic force per unit length, $F_{r,p}$. This force corresponds to a bi-dimensional geometry with a one-meter depth along the z -axis. A transformation factor was used to estimate the equivalent levitation force for a cylindrical bearing geometry, calculated by integrating the radial force projections in the angular direction, as shown in Fig. 5. When $\theta = +\pi/2$, the levitation force along the r -axis (blue vector) is equal to the radial force (red

vector), which coincides with the specific levitation force value $F_{r,p}$ from the 2D FE simulation.

The conversion factor of specific levitation force $F_{r,p}$ to the one for the cylindrical bearing geometry $F_{r,c}$ was estimated using a discrete analysis considering four sections with an arc length equal to $(\pi/8)R_{scm}$, where $R_{scm} = 0.06$ m represents the radius at the midpoint of the superconducting block ring. In Fig. 5, to calculate the radial thrust force in each section, $F_{r,p}$ (red vector) should be multiplied by the arc length of that section. The contribution of each section to the levitation force results then from the projection of $F_{r,p}$ (red vector) in the vertical r -direction (blue vector). The angle θ at the midpoint of each section was used for the projection calculation. Verifying that the total contribution for two quadrants corresponds to twice the resultant contributions of the four sections contained in one quadrant, one obtains (3) to give the conversion for the levitation forces of approximately 12.1%.

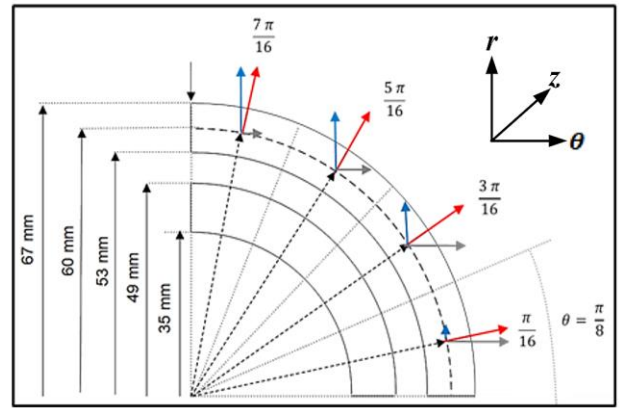


Fig. 5 Force equivalence in cylindrical geometry.

$$F_{r,c} = 2 \left(\frac{\pi}{8} 0.06 F_{r,p} \left(\sin\left(\frac{\pi}{16}\right) + \sin\left(\frac{3\pi}{16}\right) + \sin\left(\frac{5\pi}{16}\right) + \sin\left(\frac{7\pi}{16}\right) \right) \right) = 0.121 F_{r,p} \quad (3)$$

Levitation force $F_{r,c}$ varies when placing the rotor in the central position during the second magnetization step, according to Fig. 6. This depends on the vertical offset h_a for which field cooling was performed.

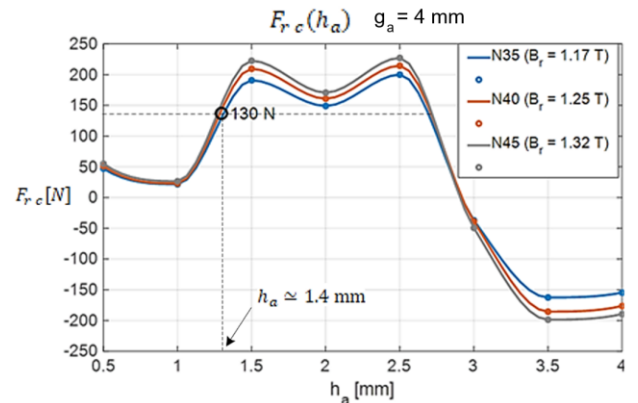


Fig. 6 Cooling height h_a to compensate for the rotor weight.

In this development, grade N40 magnets were utilized. In the central position of the rotor, the air gap between the

magnets and the superconductors is $g_a = 5$ mm. Fig. 6 shows vertical offsets h_a up to 4 mm. However, the maximum field cooling height is constrained by the thickness of the cryostat wall and the mechanical bearing limit to $h_{a_{max}} = 2.2$ mm. To achieve a levitation force of 130 N, sufficient to counterbalance the rotor's weight, 13 kg including the sleeve and magnet rings, field cooling must be performed with a vertical offset of approximately $h_a \approx 1.4$ mm.

2) *Axial magnetic forces*: The dependence of the thrust magnetic forces was also evaluated based on the axial deviations Δz of the rotor while maintaining alignment of its axis with the stator axis, after cooling at a height $h_a = 1.4$ mm. This relationship is shown in Fig. 7. The axial magnetic forces corresponding to the cylindrical geometry of the bearing F_{zc} were derived from the specific axial forces per meter associated with bi-dimensional geometry F_{zp} resulting from the 2D FEM simulation by Eq. (4). Here, $R_{scm} = 0.06$ m represents the median radius of the superconducting block ring.

The axial magnetic forces significantly exceed the levitation magnetic forces, demonstrating the inherent axial stability characteristic of the bearing.

$$F_{zc} = 2\pi R_{scm} F_{zp} \quad (4)$$

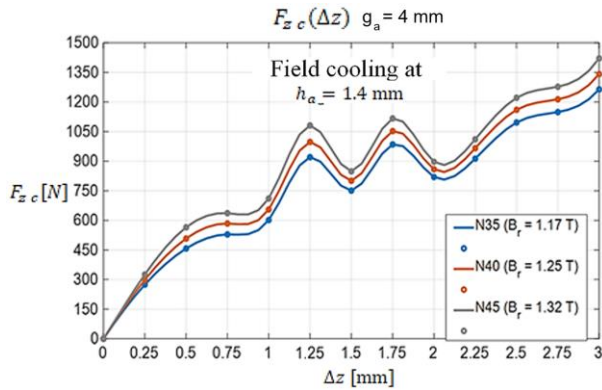


Fig. 7 Variation of the axial force F_{zc} with the displacement Δz , maintaining alignment of the rotor and stator axes after cooling with a displacement of $h_a = 1.4$ mm.

III. MOTOR AND MAGNETIC BEARING DESIGN

For the PSMB proof of concept, a conventional low-voltage induction motor with 12.5HP, 2 poles, and a frame size of 132M [11] was adopted. The air gap was increased from 0.75mm to 3.0mm, and the rolling elements bearing was designed to have a radial clearance of 2.2mm between the inner race and shaft. The shaft axial end play was 9.5mm. The induction motor data is shown below in Table I:

TABLE I
LOW VOLTAGE INDUCTION MOTOR DATA

Low voltage IM		Air gap 0.75mm	Air gap 3.0mm ^a
Rated Power (kW)		9.20	8.10
N° of poles		2	2
Rated voltage (V)		440	440
No load	I_0 (A)	6.02	17.90
	P_0 (W)	356	901
Load	I_n (A)	15.12	21.71
	P_{abs} (W)	10,194	9,468

^a Considering maximum 105K temperature increase.

A. Shaft and Bearing Rotor Designs

The magnetic rotor is composed of rings and segments of FeNdB magnets and iron rings that make up the Halbach topology [7], aiming for the highest concentration of the magnetic field. All these components are mounted on the shaft using a tubular sleeve made of AISI 304 stainless steel. The rotor constructive form is detailed in Fig. 8 and Table II.

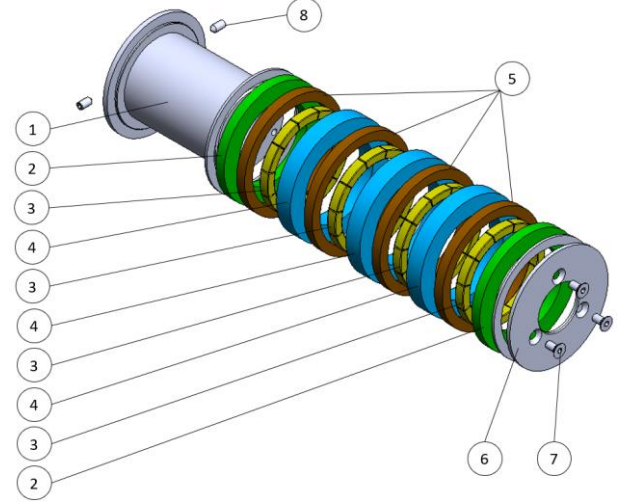


Fig. 8 Exploded view of the magnetic bearing rotor.

TABLE II
MAGNETIC BEARING ROTOR PARTS

Item	Part	Description	Qty
1	AISI 304 sleeve	To mount PMSB set on the shaft	1
2	Magnet ring A	Axial magnetization	2
3	Magnet ring B	Radial magnetization B1/B2	4
4	Magnet ring C	Axial magnetization	3
5	Ferromagnetic ring	Flux concentrator	4
6	AISI 304 cover	Rotor bearing closure	1
7	DIN 7991 - M6 x 12	Stainless steel screws	3
8	DIN 914 - M6 x 12	Stainless steel screws	2

The rings 2 (A) and 4 (C), according to the Table II and Fig. 8, are solid and have axial magnetization. The ring 3 (B) is formed from magnets segments with radial magnetization, showed in the cross section view in Fig.2.

The assembly of the three types of rings to form the magnetic rotor required an external force to press the rings against each other. Therefore, it was necessary to develop a device to contain these rings and centralize them during assembly. Once assembled, the rotor was protected with varnish against corrosion due to the presence of iron rings.

The shaft design adheres to the standard criteria for dimensions and interference fit tolerances for the motor rotor core. Only the shaft length was increased due to the PSMB rotor interface. The magnetic bearing sleeve was secured on the shaft with two screws, radially positioned 180 degrees apart, according to item 8 in the Fig. 8 and Table II.

B. Stator Bearing and Cryostat

The stator bearing consists of Yttrium Barium Copper Oxide (YBCO) superconductor blocks, which need to be cooled to achieve a superconducting state. The cryostat

plays a crucial role in the PMSB performance. The YBCO must remain in a superconducting state at 93K (-180.2 °C), which allows the use of liquid nitrogen (LN2), with a boiling point of 77K or -196°C.

The cryostat consists of one chamber for the cryogenic fluid, in this case, LN2, to remove the heat from the YBCO by conducting through the copper. The LN2 chamber is inside the cryostat tank with a vacuum chamber encompassing the entire circumferential and axial geometry to isolate the LN2 from the external environment. The cryostat cross-section view is shown in Fig. 9.

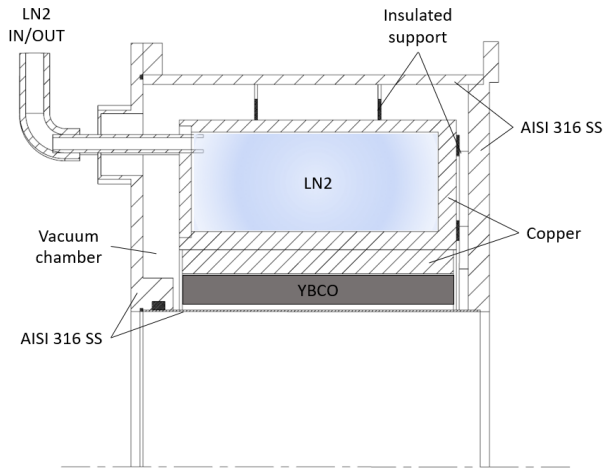


Fig. 9 Cross-section view of magnetic bearing stator (YBCO superconductor) and cryostat (cooling system)

The cryostat enclosure consists of a leakproof chamber made of AISI 316 stainless steel. This material is chosen to avoid magnetic interference with the bearing and to guarantee good protection against corrosion and oxidation caused by any water condensation.

To ensure the position of the copper chamber at the center of the cryostat tank, some radial and axial supports made by fiberglass, an insulated material, were used. Consequently, the minimum space for vacuum chamber was also ensured in the cryostat assembly. The cryostats have an inlet and outlet pipe connections for LN2 feed and an additional connection pipe for the vacuum pump system.

C. Motor Endshields and Auxiliary Bearings

Two cast iron endshields were designed and manufactured to connect the cryostat to the motor frame. These endshields have two main functions:

1. Serve as the auxiliary bearing housing to support the shaft rotor when it is landed (without cryogenic fluid).
2. Ensure the concentricity of the air gap in the magnetic bearing and the electric motor.

The auxiliary bearing is a rolling element, deep groove ball bearing, mounted on the endshield with a very slight interferent fit. The gap between the inner raceway and the shaft results in a clearance of 2.2mm.

D. Magnetic Bearing complete assembly

The complete assembly of a passive superconducting magnetic bearing for a proof of concept in a 12.5HP 2 pole motor is shown in Fig. 10.

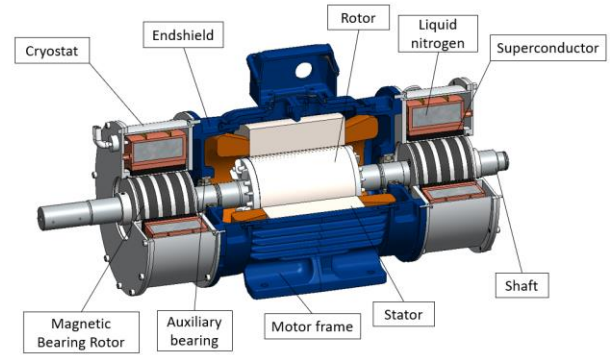


Fig. 10 Isometric cut-view of a 12.5HP electric motor with passive superconducting magnetic bearings.

IV. TEST BENCH AND RESULTS

To test the prototype's performance, two test benches were used to assess the operating point, rotor acceleration, the torque applied to the rotor, etc. Fig. 11 shows these test benches. The test bench shown in Fig. 11a was used to identify and verify the operating point, as well as to monitor the rotor's behavior as the speed changes. Load tests are performed using magnetic coupling between the prototype and the new rotating machine, as shown in Fig. 11b.

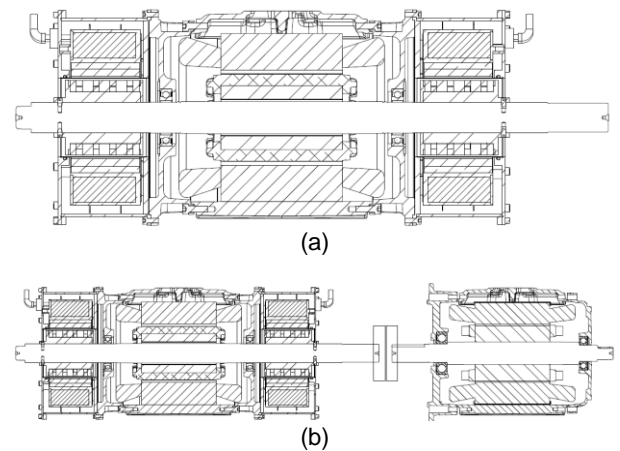


Fig. 11 Prototype test benches, (a) without load and (b) with coupling machine to simulate load.

A. Preliminary tests - no load condition

The operation of the superconducting bearing relies on positioning the rotor at the cooling point of the magnetic field. The operating process for the prototype begins with establishing an adequate vacuum within the chamber and ensuring a continuous nitrogen supply to cool the field. Nitrogen is then replenished as it is consumed (Fig. 12). After cooling, the rotor is released and operates freely. Table III presents the rotor displacement after cooling, which occurs due to the rotor's mass.

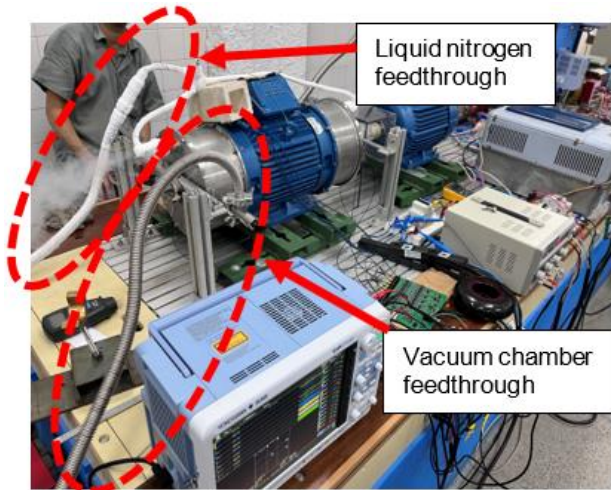


Fig. 12 Prototype operational process.

TABLE III
DISPLACEMENT OF THE ROTOR AFTER COOLING

PSMB NDE		PSMB DE	
ΔX (mm)	ΔY (mm)	ΔX (mm)	ΔY (mm)
-0.04	-0.67	-0.04	-0.47

The performance of passive superconducting magnetic bearings (PSMBs) was analyzed with the motor connected to a sinusoidal voltage supply. Initially, without coupling the motor (Fig. 11a), the stator was energized with a gradually increasing voltage, step by step, up to the nominal voltage to control the magnetic flux, Fig. 13a. This method minimizes harmonics caused by non-sinusoidal power supplies and saturation effects. It also facilitates the assessment of rotor dynamics, stator flux distribution, and the performance of the superconducting bearings. Fig. 13b illustrates the currents in each motor phase during the same voltage increment steps.

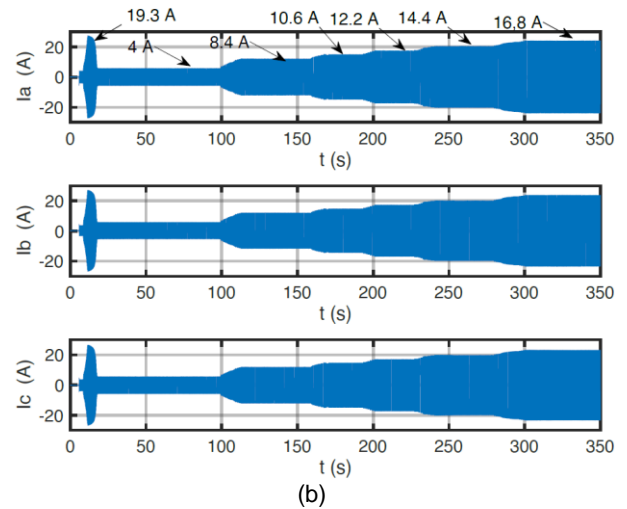
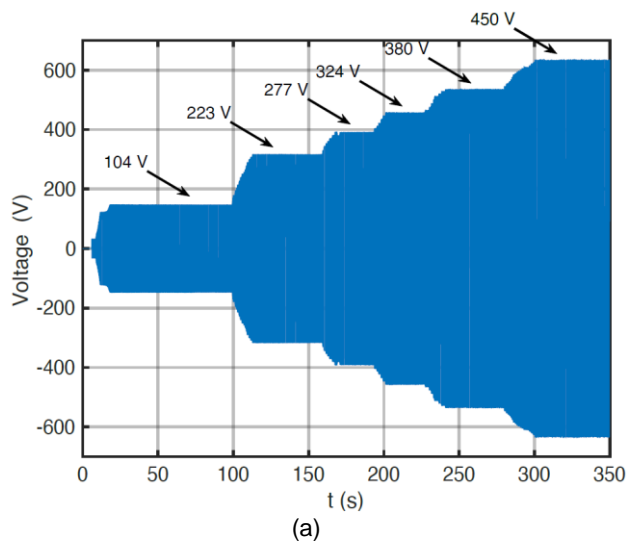


Fig. 13 Stator power supply, (a) phase a voltage and (b) three-phase currents. The values indicated by the arrows are effective RMS values.

For this case, the power supply is turned on after 6 seconds with 23 V. At this moment, the rotor starts rotating and accelerates to its nominal speed. During the acceleration process, the vibration increases in a short time as the rotor passes through the critical speed. At this stage, the stator voltage rises to 104 V, and the current is 19.3 A during acceleration, reducing to 4 A under steady-state condition. The speed at this stage is 3600 rpm.

For PSMB non-drive end (NDE), the rotor moves 0.29 mm to the right along the X-axis and 0.95 mm downward along the Y-axis, according to Fig. 14. In Fig. 15, for PSMB located on drive end (DE), the displacement is 0.18 mm to the right and 0.59 mm downward, respectively.

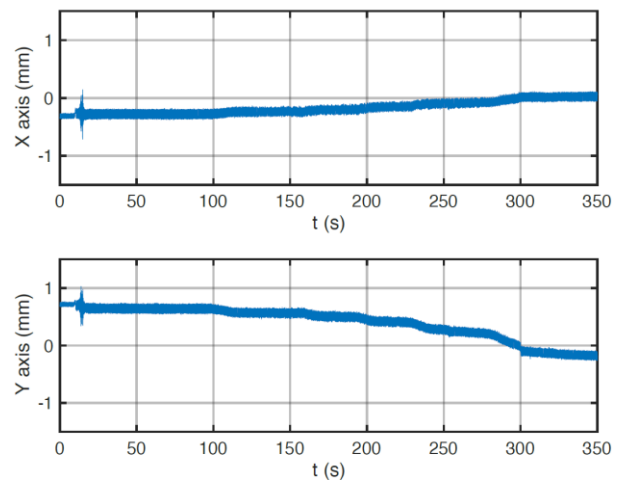


Fig. 14 Rotor behavior in PSMB NDE when the stator is supplied with a 60 Hz sinusoidal signal and stepwise voltage increments.

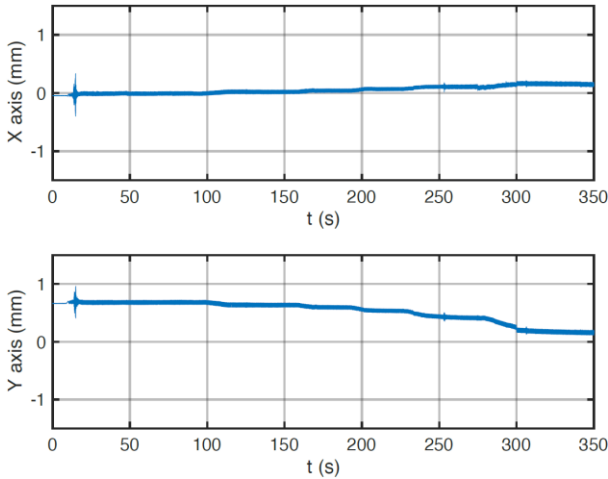


Fig. 15 Rotor behavior in PSMB DE when the stator is supplied with a 60 Hz sinusoidal signal and stepwise voltage increments.

Fig. 16 shows the X-Y graph comparing the PSMBs. Both bearings exhibit similar movement behavior, shifting to the right and downward, but with different magnitudes. This indicates a small difference in stiffness. As the system crosses the resonance frequency and the magnetic flux increases, the rotor movement remains within the safe area, which is confined to ± 1.5 on both the X and Y axes. Demonstrating good stiffness to withstand the forces generated by the motor's operation.

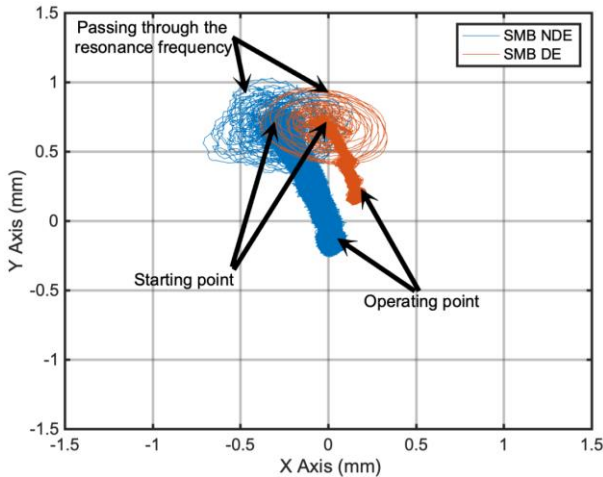


Fig. 16 Comparison of rotor movement behavior between the PSMBs.

In order to verify the behavior of the PSMBs when powered by a VSD, the prototype was subjected to a non-sinusoidal power signal and saturation effects. Figs. 17 and 18 show the rotor behavior during this test. Before this test, the mechanical rotor position was slightly shifted upward prior to cooling the superconductor. This adjustment was motivated by findings from the previous test, which revealed a downward movement of the rotor until stabilization occurred. Both magnetic bearings NDE and DE exhibited increased vibration lasting approximately 20 seconds, along with total rotor displacement since acceleration. For PSMB NDE, the rotor was displaced 0.65 mm to the right along the X-axis and 0.6 mm downward along the Y-axis (Fig. 17). For PSMB DE, the displacement was 0.46 mm to the right and 0.51 mm downward (Fig. 18).

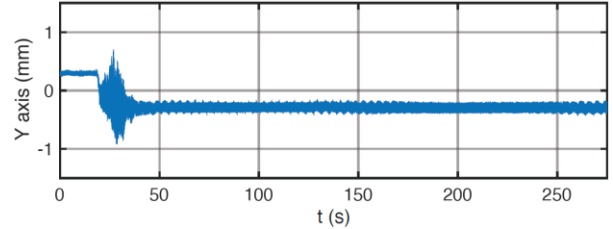
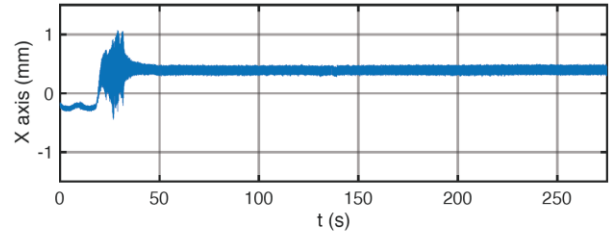


Fig. 17 Rotor behavior in PSMB NDE when the stator is supplied by a VSD.

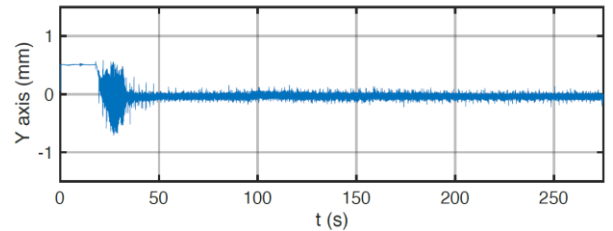
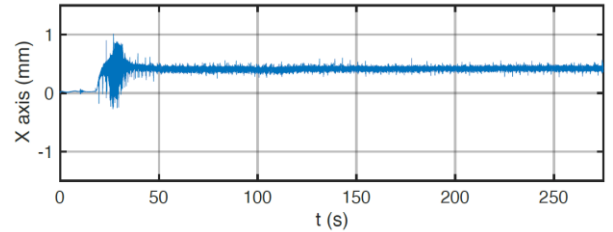


Fig. 18 Rotor behavior in PSMB DE when the stator is supplied by a VSD.

These tests allow the verification of the rotor position based on the behavior of the magnetic flux and the proper selection of field cooling in the PSMB. The variation of the magnetic flux in the motor stator causes changes in the behavior of the rotor as the flux distributes around it. For instance, the PSMB supports the weight along the Y-axis, which keeps the rotor in a stable position on this axis. However, the alteration of the motor's air gap flux changes the Unbalanced Magnetic Pull (UMP), forcing a new position of stability for the magnetic bearing, as shown in Figs. 17 and 18.

In the prototype, it is possible to compare the rotor movement downward along the Y-axis. Increasing the magnetic flux step by step moves the rotor by 0.95 mm, and when using the VSD, the rotor moves 0.6 mm for PSMB NDE. For PSMB DE, the rotor moves 0.59 mm and 0.51 mm for the flux increase steps and when using the VSD, respectively. The smaller movements observed during the VSD application can be attributed to the rotor's new position during the field cooling process. This adjustment enhances the magnetic field, resulting in stronger levitation and stabilization forces.

The rotor vibrates more significantly when the flux is powered by a VSD due to the PWM-supplied voltage, which introduces harmonics into the motor's air gap, increasing the influence of the UMP.

With the help of the VSD, it was possible to increase the rotor speed to 7000 rpm. To achieve this rotation, the magnetic flux was weakened, and the rotor displacement occurred in opposite directions when accelerated from 0 rpm to 3600 rpm. Figs. 19 and 20 show the rotor displacement as the prototype was accelerated from 3600 rpm to 7000 rpm. The rotor displacement for PSMB NDE is 0.32 mm to the left along the X-axis and 0.66 mm upward along the Y-axis. For PSMB DE, the rotor displacement is smaller: 0.20 mm to the left and 0.39 mm upward, respectively. This behavior is similar to the test with sinusoidal voltage, where the magnetic flux is increased step by step.

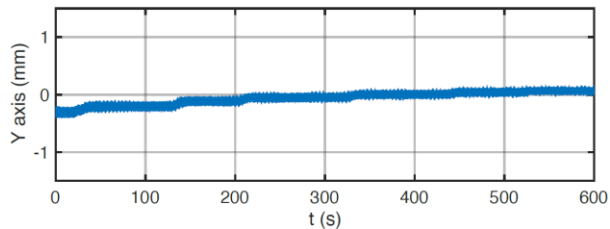
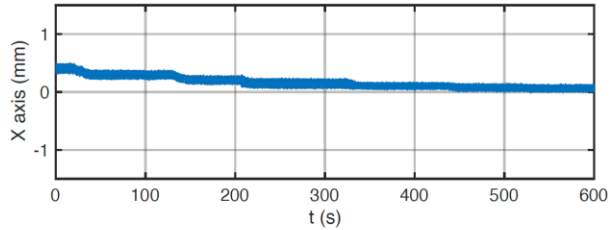


Fig. 19 Rotor behavior in PSMB NDE when the rotor is accelerated from 3600 rpm to 7000 rpm.

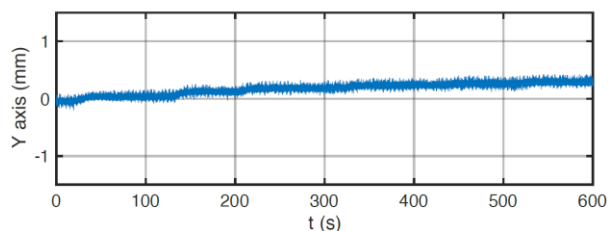
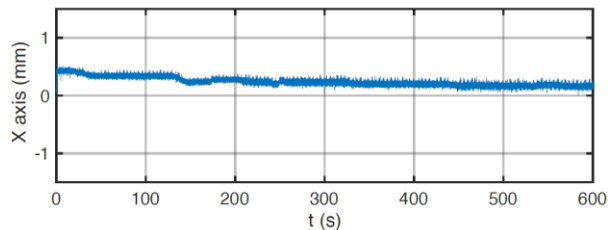


Fig. 20 Rotor behavior in PSMB DE when the rotor is accelerated from 3600 rpm to 7000 rpm.

The latest no-load test showed that a resonance frequency exists, but it is not possible to precisely identify them. Free-body tests allow for a smooth reduction in speed, making it possible to monitor the behavior of the rotor, according to Figs. 21 and 22. For PSMB NDE, when the power supply is shut down, the rotor is displaced 0.2 mm to the left along the X-axis and 0.55 mm upward along the Y-axis. During the speed reduction, the rotor maintains this position, with vibration only increasing when it crosses the resonance frequencies. For PSMB DE, the rotor is displaced 0.14 mm to the left along the X-axis and 0.4 mm upward along the Y-axis.

The resonance frequencies are similar in both bearings, and their operating range can be defined. The first resonant frequency during speed reduction is between 1550 and 1650 rpm, and the second is between 1050 and 1150 rpm.

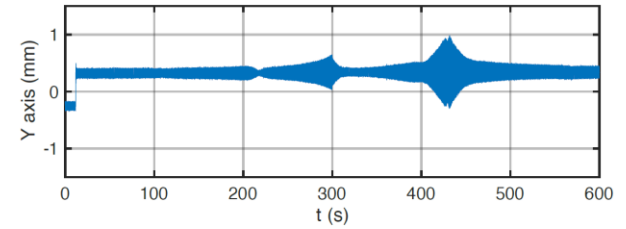
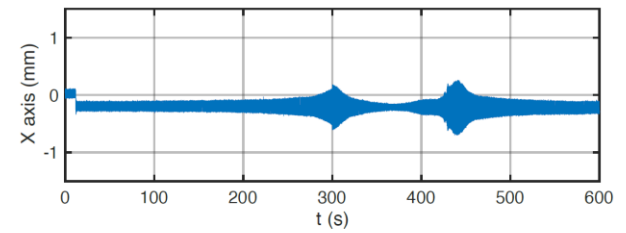


Fig. 21 Rotor behavior in PSMB NDE during free-body test.

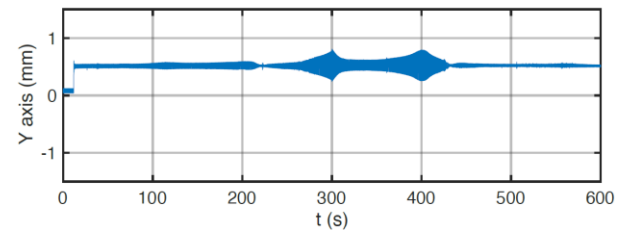
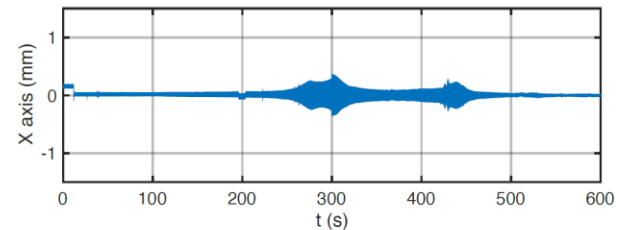


Fig. 22 Rotor behavior in PSMB DE during the free-body test.

The maximum speed of 7000 rpm was limited by the motor rotor design, mainly limited by the stress on the fans located on each side of the motor rotor core. The results showed the self-stability phenomenon of the passive superconductor bearing. Once the speed increases, more stable the PSMB becomes due to the behavior of the superconductor, in which the induced voltage depends on the speed, consequently increasing the current in the superconductor and the strength of the magnetic field.

B. Load testing of the prototype

Load testing was conducted by coupling the prototype with a rotating machine (Fig. 11b). On this test, the prototype motor with PSMB operated as a generator, and the motor drive was powered by VSD, reaching the synchronous speed of 3600 rpm. Afterward, the prototype was connected to the laboratory's electrical grid using a three-phase voltage regulator (variac).

The generator's voltage was increased to 100 V, and the current reached 4.5 A. Still, in no-load condition, the voltage was further increased to the nominal value of 440

V, and the current rose to 16.4 A, as shown in Fig. 23. The auxiliary motor, driven by VSD, increased the prototype's speed to a frequency exceeding the electrical grid's frequency (3605 rpm), which corresponds to 7.6% of the generator's nominal slip. As a result, the electric motor equipped with PMSBs began operating as a generator.

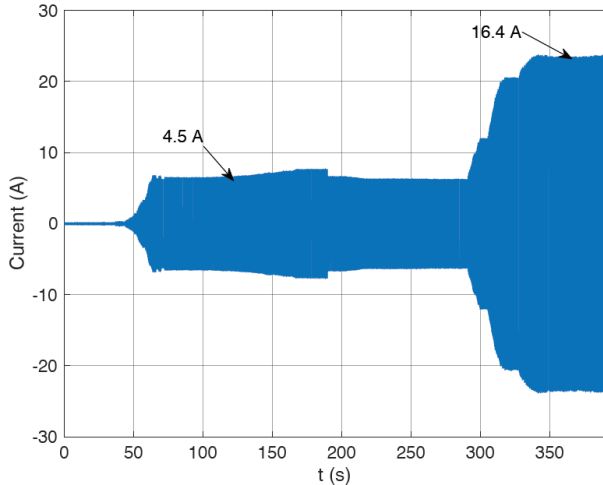


Fig. 23 Measurement of current at the prototype terminals when operating as a generator. The values indicated by the arrows are effective RMS values.

In this initial phase of the test, the prototype's operation as a generator and the stability of the bearings under 7.6% load were verified. It was observed that the rotor does not undergo significant displacements beyond those caused by passing through resonance frequencies. Since the rotor is off-center geometrically and shifted upwards, increasing the voltage to the nominal level causes magnetic forces to induce an even greater displacement of the rotor, bringing it very close to the maximum permissible limit. Fig. 25 illustrates the mechanical permissible orbit for the rotor (in blue) and the rotor's movement during loaded operation (in orange).

From this operating point, increases in the frequency of the motor controlled by the VSD were carried out, resulting in increased rotor vibration as shown in Figs. 24a and 24b for NDE and DE respectively. This increase in vibration was satisfactorily absorbed by the bearings. The NDE PSMB, even with the rotor near the maximum position of the mechanical limit, keeps the rotor within the safety zone (Fig. 25a).

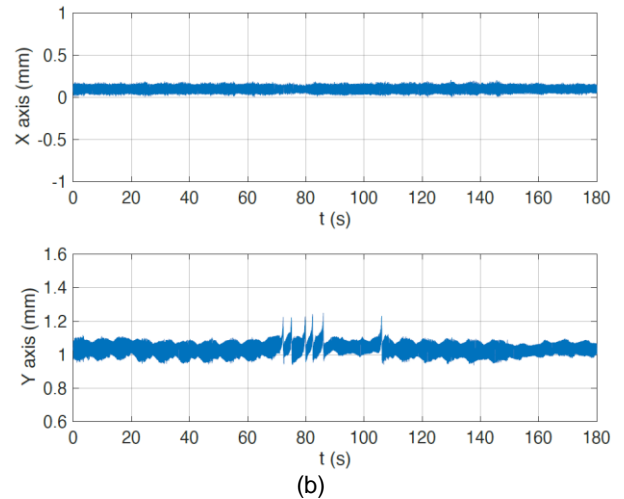
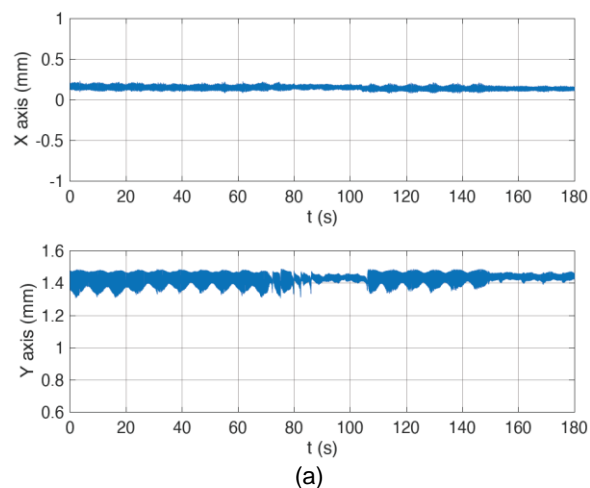


Fig. 24 Behavior of the rotor, (a) in the X and Y-axis of NDE bearing, and (b) in the X and Y-axis of DE bearing under load increase.

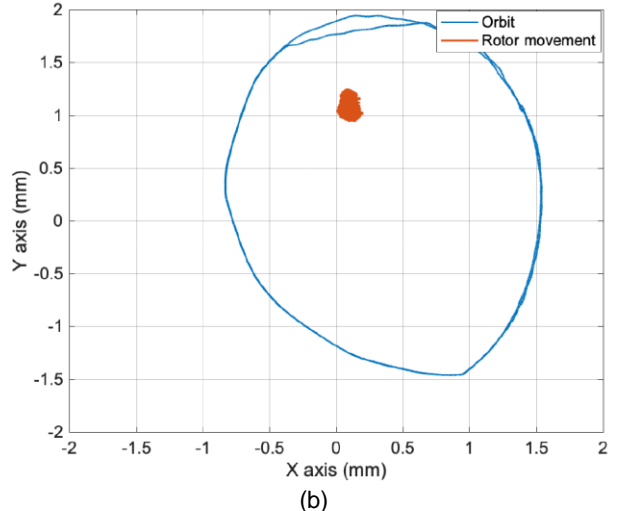
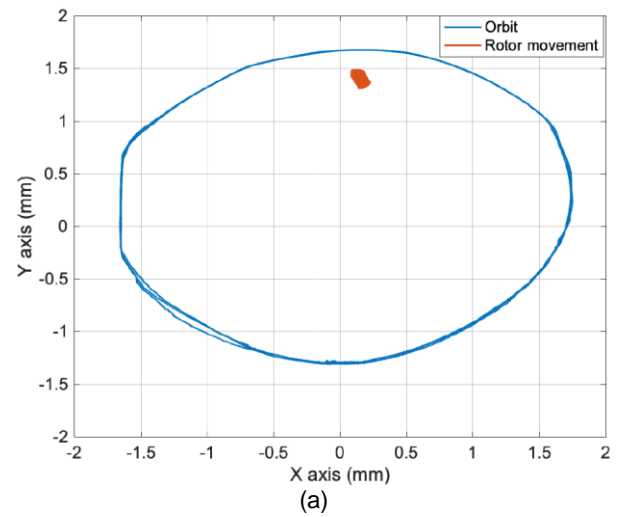


Fig. 25 Rotor's motion in (a) NDE bearing and (b) DE bearing during the load increase when the prototype operates as a generator.

Through monitoring the voltage and current generated by the prototype, it is noticeable that they remain almost constant. However, when the magnetic coupling between the two machines loses stability, variations in speed occur,

leading to fluctuations in generator performance. Due to this coupling behavior, it was not possible to apply a higher load to the generator.

New tests were proposed using a mechanical coupling with a cardan shaft. This setup allows the motor to operate under full load conditions, as well as tests at reduced load levels at higher speeds.

C. Rotor landing test

Both tests mentioned before always kept running the vacuum pump and a continuous supply of LN2 to the cryostats, which ensured the proper functioning of the bearings. In the rotor landing test, the vacuum pumps were disconnected from the cryostats, and the nitrogen supply was suspended for 15 minutes. Figs. 26a and 26b illustrates the behavior of the rotor in the NDE and DE bearings respectively.

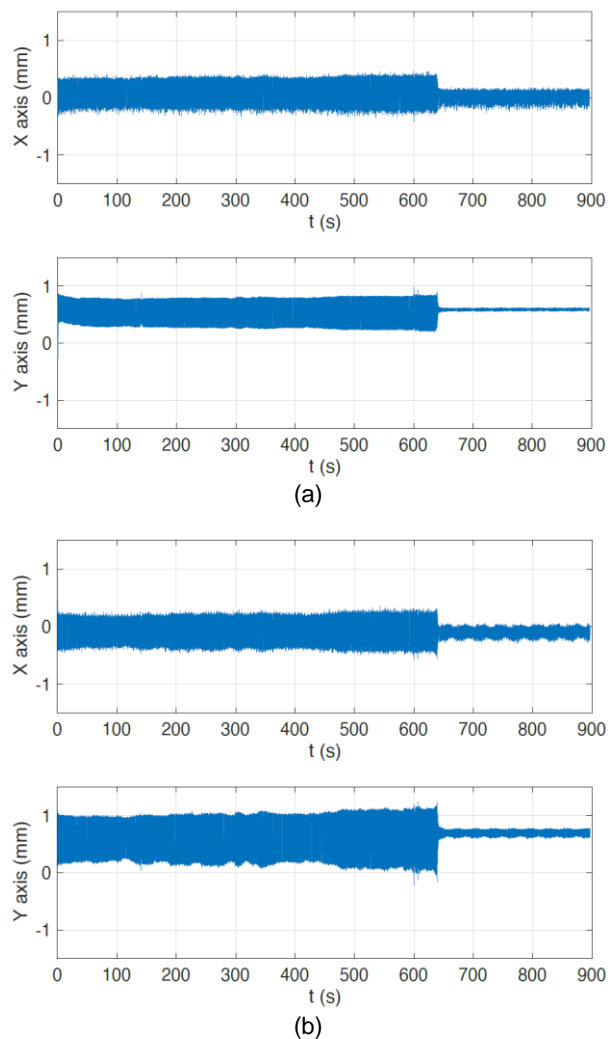


Fig. 26 Behavior of the rotor, (a) in the X and Y-axis of NDE bearing, and (b) in the X and Y-axis of DE bearing during rotor landing test

The vibration observed during the initial 640 seconds was caused by the motor operating under load, which heated the stator of the prototype, transferring heat to the cryostat. For this reason, it was decided to remove the load, which resulted in a reduction in vibration. The test continued without significant issues, with the rotor

exhibiting only a slight variation in the operating point, which did not affect the progress of the test.

During the 15 minutes of the test, the prototype operated as expected. However, shortly after, the rotor began to descend, a phenomenon that was identified and justified the process of stopping the rotor. This test confirmed that the cryostat thermal isolating issues in PSMB progress gradually and are significantly different from the rapid failures of power electronics in AMB, which are entirely dependent on auxiliary or touchdown bearings.

V. CONCLUSION

A new magnetic bearing solution was implemented in a low-voltage induction motor as a proof of concept. The superconducting effects demonstrated the self-stability of the rotor, as observed during the no-load test, where it achieved a speed of 7000 rpm, and during a limited load test, which was restricted by the coupling design.

Based on the design and test results, the following conclusions can be drawn:

- The design of the bearing based on the Halbach topology proved to be fully viable from a manufacturing point of view.
- The cryostat according to the design exposed capable of keeping the superconductor cool, however, it was deficient in thermal insulation, requiring the continuous replacement of nitrogen.
- The performance of the bearing proved to be effective both when accelerating the motor with a sinusoidal source and with a PWM source, guaranteeing the position of the motor shaft within the delimited area with a good safety margin.
- The damping of the bearing in the passage over the natural frequencies was confirmed to be excellent, both during acceleration and coast down, with similar behavior to the hydrodynamic bearings.
- The tests results showed that the positioning of the motor rotor in the axial direction was effectively maintained by the superconductors, eliminating the need for axial bearings.
- The emergency stop test revealed that touchdown bearings were not required, thanks to the delayed heating of the bearing, which ensured a prolonged rotor positioning time.
- The work demonstrated that the passive superconducting magnetic bearing is an alternative to the active magnetic bearing, but investment is still needed in the development of a closed-circuit cryostat, making the bearing industrially applicable.

VI. ACKNOWLEDGEMENTS

We extend our gratitude to Dr. Antonio Arsenio for his invaluable support in the finite element (FE) modeling of the superconductor topology. We also thank M.Sc. Felipe Costa, Prof. Dr.-Ing. Fernando C. Pinto and B.Sc. Jonatha Tavares for their significant contributions to the mechanical design and their assistance during the testing phase. Additionally, we express our appreciation to Mr. Edeval Vieira Gangá for his dedication in managing the liquid nitrogen feeding system and overseeing the test bench installation. Our thanks also go to the head of the Applied Technology Department Ms. Elissa Soares, and her team Mr. Angelo Paulucci and Mr. Welinton Trentin for their valuable discussions and efforts toward the project's

success. Lastly, we would like to acknowledge EMBRAPII for its financial support of a portion of the project.

VII. REFERENCES

- [1] Hartmut Walter, Bart Sauer and Gijs van Maanen, "Turbine Replacement with Electrical Drivers -- Evaluating Options", *PCIC energy Conference Record*, 2024
- [2] Jörg Janning, Pengcheng Zhu and Chunzhi Deng, "6MW, 10kV High Speed PMSM Digital Drive System for Highly Efficient Compressors", *PCIC energy Conference Record*, 2024
- [3] G. Schweitzer and E. Maslen, "Magnetic Bearings: Theory, Design and Application to Rotating Machinery", *Springer*, 2010.
- [4] F. Moon, "Superconducting Levitation: Applications to Bearings and Magnetic Transportation", Wiley, 2008.
- [5] R.M. Stephan, F. Costa, "Superconducting Magnetic Levitation (SML): a new generation of urban MagLev vehicles", *26th International Symposium on Magnetically Levitated Systems and Linear Drives*, Malmö, September 2024.
- [6] European Association of Research and Technology Organisations, The TRL Scale as a Research and Innovation Policy Tool; EARTO: Brussels, Belgium, 2014.
- [7] G. G. Sotelo, A. C. Ferreira, and R. de Andrade Jr. "Halbach Array Superconducting Magnetic Bearing for a Flywheel Energy Storage System". *IEEE Transactions on Applied Superconductivity*, pp 2253-2256, 2005
- [8] Z. Hong, A. M. Campbell, and T. A. Coombs. Computer Modeling of Magnetization in High Temperature Superconductors. In *IEEE Transactions on Applied Superconductivity*, 17(2), pp. 3761-3764, 2007.
- [9] Z Hong, A M Campbell, and T. A. Coombs. Numerical solution of critical state in superconductivity by finite element software. In *Superconductor Science and Technology*, vol. 19, no. 12, pp. 1246–1252, 2006.
- [10] Zhang, Min, and T. A. Coombs. "3D modeling of high-Tc superconductors by finite element software.". In *Superconductor Science and Technology*, vol. 25, no. 1, 015009, pp. 1-7, 2012.
- [11] IEC 60072-1 Rotating electrical machines – Dimensions and output series – Part 1: Frame numbers 56 to 400 and flange numbers 55 to 1080

VIII. VITA

Gabriel Chagas Storti graduated from Universidade Federal do Rio Grande (FURG), Brazil in 2008 with a B.Sc. in Mechanical Engineering degree. After graduation he joined WEG Energy in Jaraguá do Sul / Brazil working as a mechanical engineer specializing in turbo and hydro generators. Since 2014 he has been dedicated to bearing technologies, focusing on developing innovative solutions for electric rotating machines at Development & Technological Innovation department (D&IT).
storti@weg.net

Fredemar Rüncos received the Engineering and Physics degrees from the Federal University of Paraná, Brazil in 1980. In 2002 and 2006 he received his M.Sc. and Ph.D. degrees in electrical engineering, respectively, from the

Federal University of Santa Catarina, Brazil. In 1990 he became the manager of the product engineering department of WEG Energy for large rotating electrical machines. In 2009 He became manager of the D&TI department of WEG Energy. At present, he is a D&TI consultant and Professor in the electrical engineering department of the Catholic University Center of Santa Catarina. His research interests surround induction and synchronous machines, including developing methods to analyze the performance and vibration, design criteria and control of a Brushless double fed induction machine with rotary transformer and permanent magnet synchronous machines.
fredemar@weg.net

Richard M. Stephan received the Engineering degree from Instituto Militar de Engenharia (IME), Rio de Janeiro, in 1976, the M.Sc. degree from Universidade Federal do Rio de Janeiro (UFRJ) in 1980, and the Dr.-Ing. degree from Ruhr Universität Bochum, Germany, in 1985; all in Electrical Engineering. Since 1978, he has been with the Department of Electrical Engineering, UFRJ. His main interests are in the fields of applications of superconductivity, MagLev technology, control of electrical drives and power electronics. Dr. Stephan is a former president of SOBRAEP (Brazilian Society of Power Electronics). He is Senior Researcher of CNPq, Senior Member of IEEE and, since 2019, member of the Brazilian Academy of Engineering.
richard@dee.ufrj.br

Elkin Ferney Rodriguez received the Dipl.-Eng. degree in Electronic Engineering from "Los Libertadores" University, Bogotá, Colombia, in 2003, and the M.Sc. and D.Sc. degrees in Mechanical Engineering from the Fluminense Federal University in 2006 and 2010, respectively. Since 2014, he has been a professor in the Department of Electrical Engineering at UFRJ. His research focuses mainly on the following topics: motors with magnetic bearings, self-bearing motor, passive magnetic levitation, sensors, electrical machines, and control systems, including vector control.
elkin@dee.ufrj.br

Paulo Branco is a Full Professor in Energy at IST, University of Lisboa. He is the Deputy Coordinator and Researcher at the Center for Intelligent Systems. With 30 years of pedagogical activity, he has contributed significantly to various engineering programs at IST, including Electrical and Computer Engineering, Energy Management, and Aerospace Engineering. He has also initiated several key curricular units and held administrative roles, including overseeing the Electric Machines Laboratory. His research focuses on photovoltaic system optimization, energy efficiency in induction generators, smart grid reliability using "fuzzy" logic, and advanced ferromagnetic and superconducting materials for electric and hybrid propulsion systems.
pbranco@tecnico.ulisboa.pt